



Monitoring Diffuse Volcanic Degassing with Seismic Ambient Noise

Helena Seivane^{1,2}, Martin Schimmel¹

¹Geosciences Barcelona (GEO3BCN, CSIC), Lluis Solé i Sabarís s/n, Barcelona, Spain ²Institute of Marine Sciences (ICM, CSIC), Passeig Marítim de la Barceloneta 37-49, Barcelona, Spain

Correspondence to: Helena Seivane (helenaseiv@outlook.com)

Abstract. Diffuse volcanic degassing is a persistent and often underestimated natural hazard, with potential impacts on air quality, ecosystem health, and volcanic risk management. Detecting and monitoring this process is challenging, especially in volcanoes lacking visible fumarolic activity, where the final stage of gas migration is jointly modulated by the shallow subsurface structure and natural pressure forcings. We present a continuous monitoring approach based on Rayleigh wave ellipticity from ambient seismic noise to track pressure-driven gas transport in the uppermost soil layers. Applied to Cumbre Vieja Volcano (La Palma, Canary Islands), the method detects subdaily seismic velocity variations linked to periodic pressure oscillations, consistent with natural forcings such as atmospheric and solid earth tides. In this work, we focus on the terdiurnal cycle, the only subdaily band at La Palma Island that reflects purely atmospheric pressure forcing. Its temporal evolution reveals long-term fluctuations that broadly coincide with reported CO2 emission trends, despite differences in spatial and temporal resolution between both estimates. In addition, we identify a clear semi-annual cycle in the long-term ellipticity response at the terdiurnal frequency. This seasonality coincides with the modulation by solid Earth tides and confirms their role in controlling permeability in the upper vadose zone and in the enhancement of barometric pumping efficiency across all stations analyzed. Prior to the 2021 eruption, the terdiurnal cycle reveals contrasting station responses, with TBT exhibiting the earliest and most sustained increase. Together, these observations point to the usefulness of this approach as a complementary tool in the assessment of diffuse degassing and volcanic unrest. This seismic-noise-based approach offers a cost-effective and resilient strategy for detecting hazardous gas migration, supporting early warning and mitigation efforts in volcanic regions.

25 1 Introduction

15

20

Diffuse volcanic degassing is the continuous, nonvisible release of gases from a volcanic system through soil, fractures, and other permeable structures, occurring even during quiescent periods and independently of fumaroles or plumes. Anomalies in this process can represent both a precursor of volcanic activity and a geohazard. However, detecting this subtle volcanic manifestation is challenging due to typically low emission fluxes and the need for specialized instrumentation (Viveiros and Silva, 2024). Among the released gases, carbon dioxide (CO₂) and helium (He) are key indicators of magmatic activity, as elevated emissions often precede magma ascent. Despite this, degassing anomalies prior to eruptions remain rare (e.g.,



45



Hernández et al., 2001; Pérez et al., 2022). Therefore, their long- to medium-term monitoring is crucial for improving volcanic hazard assessment and early warning capabilities (Epiard et al., 2017).

The final stage of volcanic gas transport occurs in the vadose zone, the unsaturated region between the water table and the surface, where periodic natural pressure forcings can modulate gas movement. In coastal volcanic settings, these forcings may arise from barometric tides, ocean tides transmitted through hydraulically connected aquifers, and solid Earth tides, each contributing to poroelastic deformation and pore pressure changes with distinct amplitudes, phases, and penetration depths (e.g., Wang and Manga, 2021; Sato, 2005; Jiao and Li, 2004; Merrit, 2004; Robinson and Bell, 1971). This study targets the atmospheric tidal component by focusing on the upper vadose zone, where gas-phase processes dominate and barometrically induced pressure serves as a proxy for gas transport.

To test this approach, we apply Rayleigh wave ellipticity (RWE) from ambient seismic noise as a high-resolution near-surface monitoring tool (e.g., Seivane et al., 2024) to track gas accumulation at Cumbre Vieja, La Palma. Unlike other volcanic islands with widespread visible degassing, La Palma exhibits limited surface gas emissions, with the only known manifestation being a CO₂-rich bubbling cold spring in the Taburiente caldera (Padrón et al., 2015). This unique setting offers ideal conditions to investigate diffuse degassing and to evaluate barometric pumping as a mechanism for detecting subsurface gas accumulation at timescales and depths not yet addressed by existing seismic monitoring networks, with direct implications for improving hazard assessment during volcanic unrest.

Previous studies using seismic noise interferometry in La Palma (e.g., Cabrera-Pérez et al., 2023a; Mezcua and Rueda, 2023) have focused on deeper structures. Therefore, monitoring the vadose zone requires a shift in both spatial and temporal scales.

This study targets the very near surface, where periodic hourly cycles associated with barometric pumping are known to modulate the rates and magnitudes of gas exhalation (e.g., Forde et al., 2019). Such short-term variations cannot be effectively resolved using ambient noise interferometry with the current seismic network in La Palma, as its station density and frequency resolution are insufficient for detecting these near-surface processes. Dense seismic arrays with inter-station distances ranging from hundreds of meters to a few kilometers have demonstrated this capability (Kramer et al., 2023), but their availability is often limited. In this study, we address the limitations in spatial resolution and sensor requirements of previous approaches by applying RWE as an alternative seismic-noise-based method to detect pressure-driven processes and assess their role in diffuse degassing





60 2 Study Area

75

80

90

La Palma, one of the most volcanically active islands in the Canary Archipelago, is composed of two main volcanic structures: the circular shield volcano of Taburiente in the north and the elongated Cumbre Vieja rift to the south (Figure 1). These volcanoes become progressively younger from north to south, reflecting the continuous migration of emerged volcanism in this direction (Carracedo et al., 2001; Troll and Carracedo, 2016).

Unlike other volcanic islands, La Palma lacks visible fumarolic emissions. However, the N-S rift system is known to serve as a major pathway for deep gas migration and diffuse degassing, with He emissions confirming mantle-derived contributions (Padrón et al. 2012). The island's hydrogeological system is highly compartmentalized, controlled by the rift structure and a dense network of magmatic dikes that extend from the Basal Complex to the most recent basaltic deposits (Poncela et al. 2022). These dikes act as hydrological barriers, influencing groundwater stratification and creating steep piezometric gradients, while also enhancing gas exchange and ventilation within the vadose zone (García-Gil et al. 2023). As noted by Nilson et al. (1991), the presence of fractures in porous media facilitates the propagation of pressure variations, enabling the gas movement from greater depths. Therefore, natural pressure forcings are not the only controlling factor. Gas transport efficiency also depends on porosity, permeability, water content, and other structural and hydrological characteristics.

The vadose zone in La Palma varies significantly in thickness (Poncela et al. 2022). In the Barranco de las Angustias, where groundwater levels are high and perennial runoff occurs—an exceptional case on the island—it is only a few meters thick. In contrast, in the central rift zone, where groundwater lies deeper, it extends several hundred meters. Porosity and permeability depend on the age, compaction, and degree of fracturing of volcanic materials. In Cumbre Vieja, younger basaltic flows exhibit higher porosity and permeability than the older, more compacted basalts of Taburiente (Figure 1). Lastly, vertical dike intrusions, abundant in the Taburiente Caldera and affecting the basal complex, act as structural controls on fluid and gas migration. They enhance vertical permeability while reducing it perpendicular to their orientation.

The 2021 eruption of Cumbre Vieja, preceded by years of deep seismicity (25–35 km) since 2017, was marked by a rapid escalation of unrest. Seismicity migrated from 10 km depth to shallower levels beginning on September 11, 2021, accompanied by clear deformation signals. A progressive decrease in seismic velocity (dv/v) was recorded 9.5 days before the eruption (Cabrera-Pérez et al. 2023a), localized near the future eruptive centers and associated with a cluster of shallow earthquakes (<4 km) that appeared only four days before. This pattern suggests hydrothermal fluids released by ascending magma reached the surface ahead of the magma itself (Carvalho et al., 2024; Cabrera-Pérez et al., 2023a). This aligns with the dual magma ascent pathways proposed by Mezcua and Rueda (2023), where magma rose from a lower crustal reservoir (~11 km) from September 12–14, with an accelerated ascent from 4 km depth prior to the eruption, a process linked to both magma-driven deformation and hydrothermal fluid migration (Cabrera-Pérez et al. 2023a). The eruption began on September 19, lasted 85 days, destroyed over 2800 buildings, and covered nearly 1000 hectares with lava and pyroclasts. While the dv/v



100

105



anomaly provided crucial early warning signals, strong volcanic tremor during the eruption limited the applicability of ambient noise interferometry for real-time monitoring.

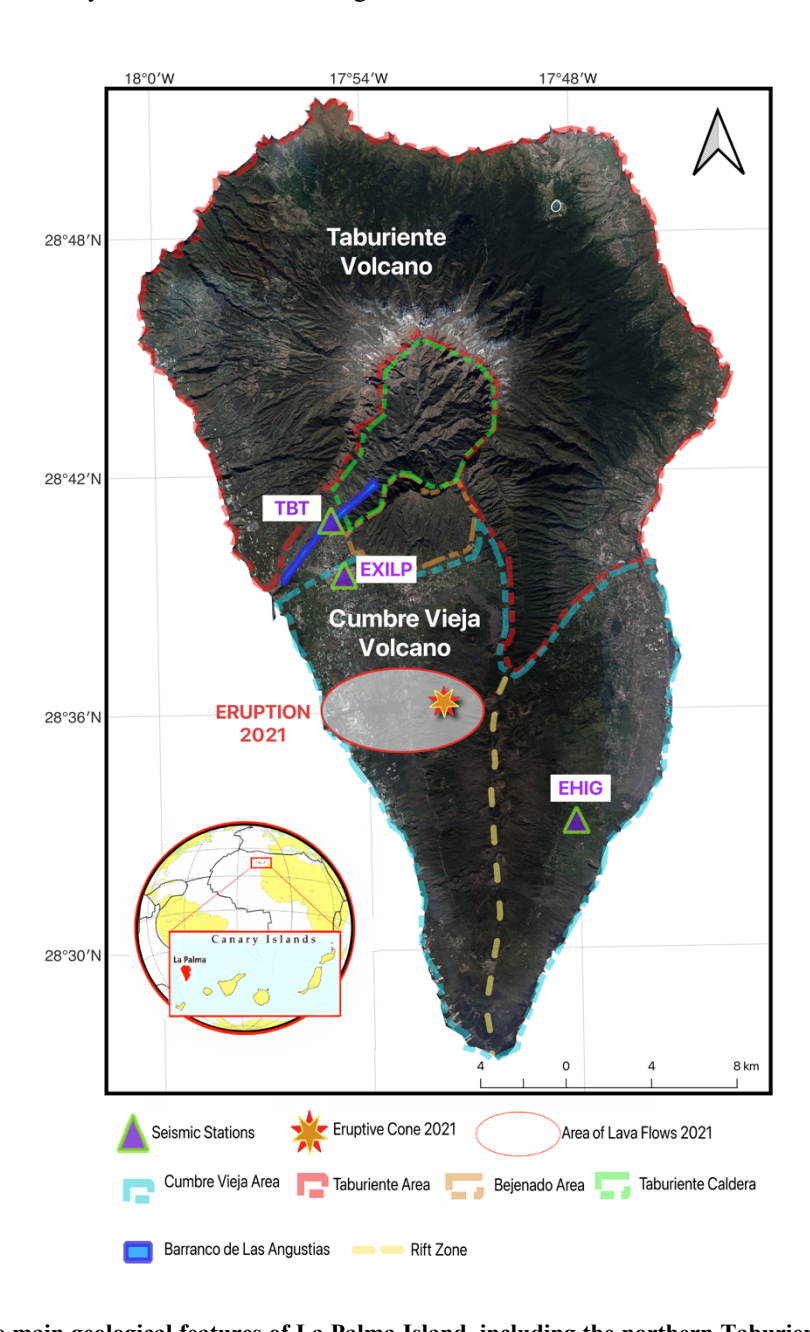


Figure 1. Map of the main geological features of La Palma Island, including the northern Taburiente and Bejenado volcanoes, the
Taburiente Caldera, and the southern Cumbre Vieja Volcano with its rift zone. The seismic stations used in this study are represented by violet-green triangles, and the area affected by the 2021 eruption is also highlighted. The background orthophoto of La Palma is based on OrtoPNOA 2024 (CC-BY scne.es), with modifications by the authors.



125

130

135

140



3 Materials and Methods

3.1 Gas-Phase Flow under Atmospheric Pressure Forcings

Daily fluctuations in atmospheric pressure, known as atmospheric tides, result from the absorption of solar radiation in the upper atmosphere. These tides are oscillations with periods which correspond to integer fractions of a solar day, primarily at 24 hours (diurnal), 12 hours (semidiurnal), and 8 hours (terdiurnal). These variations can induce periodic pressure changes in the Earth's subsurface, which can drive subsurface gas movement through porous and fractured earth materials—a process known as barometric pumping. This phenomenon has been widely studied in diverse contexts, including contaminant transport, gas leakage in oil and gas wells, and cave ventilation (e.g., Auer et al., 1996; Forde et al., 2019; Gomell et al., 2021).

The efficiency of barometric pumping in mobilizing subsurface gases depends on the physical properties of the porous medium and surrounding conditions. In environments where the pore space is predominantly gas-filled with negligible liquid water, gas flow can be treated as single-phase. This condition is commonly met in the upper vadose zone, where gas dominates and water content remains low. In practice, true steady-state flow is rarely achieved in subsurface gas transport. Instead, gas movement typically occurs under transient flow conditions, where pressure, density, and flow rate fluctuate over space and time. This behavior is governed by a diffusion-type partial differential equation, mathematically analogous to heat conduction in solids or solute diffusion in liquids. Unlike these stochastic processes, pressure diffusion in porous media follows Darcy's law, which describes fluid movement through a porous matrix. Mathematically, Darcy's law is analogous to fundamental transport laws such as Ohm's law for electrical conduction, Fick's law for solute diffusion, and Fourier's law for heat conduction (Zimmerman 2018).

The governing equation for pressure diffusion in porous media results from coupling Darcy's law with mass conservation (e.g. Lin, 1977; Brace et al., 1968). Under isothermal conditions, assuming one-dimensional transient gas flow in a homogeneous and isotropic medium, the governing equation is expressed as a nonlinear partial differential equation

$$\frac{\partial P}{\partial t} = \frac{k}{\phi \mu c_t} \frac{\partial^2 P}{\partial z^2} \tag{1}$$

where P is the gas pressure, t is time, z is the vertical coordinate, k is the medium permeability, ϕ the medium porosity, ϕ the medium porosity, ϕ the medium ϕ and ϕ compressibilities ϕ compressibilities ϕ and ϕ like ϕ compressibilities ϕ like ϕ lin ϕ like ϕ like ϕ like ϕ like ϕ like ϕ like ϕ like





$$D = \frac{k}{\phi \mu c_t} \tag{2}$$

The analytical solution for Equation 1, taking as a boundary condition the surface pressure caused by the atmospheric tides

$$P(z=0,t) = P_0 \cos \omega t \tag{3}$$

can be expressed as

150

155

145
$$P(z,t) = P_0 e^{-z\sqrt{\omega/2D}} \cos(\omega t - z\sqrt{\omega/2D})$$
 (4)

where ω is the frequency of the atmospheric fluctuations (Hanks and Woodruff, 1958).

In the context of diffuse degassing, the injection of gas into the vadose zone alters the system's compressibility and, consequently, the subsurface response to atmospheric pressure oscillations. The total compressibility, defined as $c_t = c_m + c_g$, determines the rate at which pressure propagates through the medium. As gas concentration increases, the gas compressibility c_g decreases, reducing c_t and thereby increasing hydraulic diffusivity D (Equation 2). This enhancement in diffusivity facilitates the deeper penetration of atmospheric pressure oscillations into the subsurface.

Equation (4) shows that both amplitude attenuation and phase shift depend on D. An increase in D reduces attenuation and decreases the phase lag with depth, while a decrease in D has the opposite effect. However, when multiple natural forcings act simultaneously and induce pressure oscillations in the subsurface (e.g., atmospheric tides, solid earth tides, and aquifer fluctuations), changes in the observed amplitude may not exclusively reflect variations in diffusivity but can also result from the superposition of different forcings (e.g., Kuang et al. 2013). To minimize the ambiguity associated with the concurrent action of multiple natural forcings in the subsurface, we focus on the analysis of subdaily tidal bands as the most robust indicators of atmospheric forcing.

3.2 Monitoring of Seismic Velocity Variations through Rayleigh wave Ellipticity

The particle motion of Rayleigh waves is polarized along a vertical ellipse, whose ellipticity—defined as the ratio between its horizontal and vertical axes—is highly sensitive to the subsurface structure beneath and around the seismic station where it is measured (e.g., Maupin, 2017; Cercato, 2018). Compared to traditional methods relying on continuous cross-correlation of ambient seismic noise, monitoring subsurface velocity variations using RWE offers two key advantages: (1) its sensitivity kernels are well-constrained and easily derived across different frequency bands, ensuring reliable depth sensitivity, and (2) it



170



is unaffected by noise source variability, making it particularly robust for real-time monitoring, even during tremor episodes. The effectiveness of this approach has been confirmed by Seivane et al. (2024), who demonstrated its applicability across various geological contexts, specially focusing on the monitoring of shallow structures.

As a general procedure for each analyzed seismic station, and following the workflow proposed by Seivane et al. (2024), we first apply the DOP-E method (Schimmel and Gallart, 2003; Berbellini et al., 2019) to retrieve the RWE function using a 2-hour sampling interval. Instead of computing the Dissimilarity Index (DSI), we directly analyze the raw ellipticity variations as a function of frequency and time. This frequency-by-frequency approach allows us to retain the full spectral resolution of the ellipticity function and to identify narrow-band periodic signals. Compared to the DSI-based methodology presented in Seivane et al. (2024), the direct analysis of ellipticity variations improves sensitivity to localized changes concentrated in single frequencies or specific frequency ranges.

A comparable alternative to RWE is the horizontal-to-vertical spectral noise ratio (HVSNR) method, which has demonstrated similar sensitivity to velocity variations associated with groundwater dynamics (Seivane et al., 2022; Vassallo et al., 2022; Galone et al., 2024). However, the HVSNR method is highly dependent on wavefield composition (see Figure A1 in Appendix) and can be significantly affected by transient disturbances (Hagshenas et al. 2008). Consequently, its applicability for continuous structural monitoring during tremor episodes is constrained by the same limitations, i.e. wavefield variability, that affect ambient noise interferometry (e.g., Sánchez-Pastor et al., 2018; Cabrera-Pérez et al., 2023a; Carvalho et al., 2024).

The sensitivity of RWE to perturbations in the elastodynamic parameters that define the subsurface structure, typically modeled as multiple layers with associated shear wave velocity (V_s), compressional wave velocity (V_p), and density (ρ), has been shown to be more strongly influenced by variations in V_s than by changes in V_p or ρ (e.g., Maupin, 2017; Cercato, 2018). However, given that this study focuses on the unsaturated vadose zone and its response to gas injections, we anticipate a phenomenon where V_p undergoes more significant variations than V_s (e.g., Sánchez-Pastor et al. 2023). According to Conte et al. (2009), the V_s and V_p for unsaturated and dry conditions, in a regime where the relative motion between gas and solid phases is negligible, can be expressed as:

$$V_s^2 = \frac{G}{(1-\phi)\rho_S + \phi\rho_g},\tag{5}$$

190 and

$$V_P^2 = \frac{(2G(1-\nu^{SK})/(1-2\nu^{SK})) + (K^g/\phi)}{(1-\phi)\rho_S + \phi\rho_g},\tag{6}$$





Where G is the shear modulus, ϕ is the porosity, v^{SK} is Poisson's ratio of the soil skeleton, K^g denothes the bulk modulus of the gas filling the soil pores, ρ_a and ρ_s are the densities of gas and solid phases.

An input of additional gas into the pore space will increase the gas density ρ_g , which will slightly raise the overall bulk density of the medium. As shown in Equation (5), this will result in a slight decrease in V_S since the shear modulus G remains unchanged, while the denominator increases due to the higher gas density. In contrast, the effect on V_P is determined by the balance between changes in bulk modulus and density. The bulk modulus varies with the rate of pressure change relative to volume, i.e., $K^g \propto \frac{\partial P}{\partial V}$. According to Equation (6), an increase in bulk modulus leads to a rise in V_P , meaning that the pressure oscillations driven by barometric pumping will induce cyclic variations in V_P on daily timescales.

While RWE alone does not inherently distinguish between variations in V_P and V_S, analyzing the effects of barometric pumping allows us to confidently attribute the observed variations to V_P changes, as periodic pressure modulations in the upper vadose zone affect the bulk modulus rather than the shear modulus. Moreover, without direct velocity measurements or a precise understanding of the underlying mechanism, RWE alone does not indicate whether velocity increases or decreases. While a reliable proxy for variations, its interpretation must be case-specific, accounting for underlying physical processes.

4. Results and Discussion

205

210

To demonstrate the impact of gas injections from diffuse volcanic activity on the upper vadose zone and the ability of RWE to monitor these changes, we analyzed the long-term record (2007–2023) of the EHIG seismic station (Figure 1). This station is particularly suited for our study because it was operative during the well-documented episode of increased diffuse CO₂ emissions reported by Padrón et al. (2015) between 2007 and 2012, and it continued recording throughout subsequent volcanic unrest and the 2021 eruption. Although pre-eruptive swarms in 2021 were accompanied by reports of enhanced degassing (e.g., Santana de León et al., 2022), the lack of quantitative CO₂ flux data prevents direct comparison for that period.

The most robust strategy to confidently isolate the atmospheric contribution from other possible forcings is to focus on the 8215 hour atmospheric tide, which is clearly expressed in the atmospheric pressure spectrum, while the corresponding 8-hour oceanic, solid Earth, and temperature tidal constituents are nearly absent (Figure 2). This spectral separation makes the 8-hour signal a reliable diagnostic of barometric forcing. In La Palma, the 8-hour barometric tide has an amplitude about five times smaller than the dominant 12-hour component (Figure 2), whereas the 8-hour ocean tide (M₃) is nearly three orders of magnitude weaker than the principal 12-hour ocean tide (M₂) (Dirección General de Costas, 2004), further reinforcing its suitability as a barometric indicator.



225



Figure 3a shows the spectrogram of the RWE series at station EHIG in the 0.8–5 cycles per day (cpd) band. To construct this figure, the RWE time series at each analyzed frequency for one representative year within the full record (2007–2023) was segmented into overlapping 30-day windows. Within each window, the mean was removed and a fast Fourier transform (FFT) was applied to obtain the frequency spectrum of the detrended signal. At station EHIG, the dominant spectral peaks occur at 1 and 2 cpd (hereafter E₁ and E₂), confined to the 40–50 Hz frequency range. In addition, weaker but well-defined peaks appear at 3 and 4 cpd (E₃ and E₄) between 45 and 50 Hz. The long-term spectrogram of the 48 Hz RWE series (Figure 3b) confirms the persistence of all four components (E₁–E₄) throughout 2007–2023, corresponding to periods of 24, 12, 8, and 6 hours, respectively.

To investigate the link between RWE and known tidal forcings, we calculated the magnitude-squared coherence (MSC) between RWE and potential external drivers: atmospheric pressure and temperature time series derived from the ERA5 reanalysis database, and vertical solid Earth tides computed with the Python package pysolid (Yunjun et al. 2022). MSC quantifies, in the frequency domain, the linear correlation between two time series through their cross-spectra, and helps identify phase and amplitude synchronizations. It is defined as:

$$\gamma_{xy}^{2}(f) = \frac{|P_{xy}(f)|^{2}}{P_{xx}(f) \cdot P_{yy}(f)}$$
(7)

Where $P_{xx}(f)$ and $P_{yy}(f)$ are the power spectral densities (PSD) of the two time-series, and $P_{xy}(f)$ is their cross-spectral density. We estimated MSC using Welch PSD method (Welch 1967), as implemented in the MATLAB function pwelch. The RWE and driver series were resampled at 2 h intervals, segmented into overlapping windows of 60 days, tapered with a Hanning window, and averaged in the frequency domain.

240





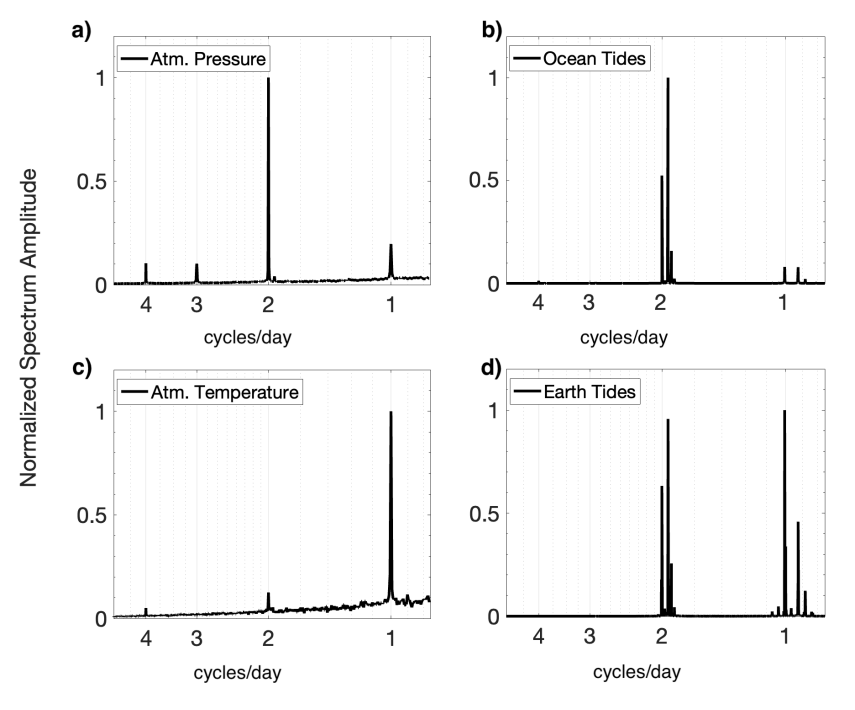


Figure 2. Normalized amplitude spectra obtained from the Fourier transform of: a) atmospheric pressure time series retrieved from ERA5 (https://cds.climate.copernicus.eu/datasets/), b) ocean tide time series reconstructed from the harmonic constituents of Tazacorte Port (Dirección General de Costas, 2004), c) atmospheric temperature time series from ERA5, and d) vertical solid Earth tide displacement for La Palma Island derived with pysolid (Yunjun et al. 2022).

The MSC spectra shown in Figure 3c for the RWE function at 48 Hz compared to the three different tidal forcings prove that
the observed spectral peaks in RWE (Figure 3 a-b) are statistically significant and highly correlated with the external drivers.
However, statistically significant coherence does not necessarily imply a causal relationship. For instance, in the MSC between RWE at 48 Hz and the vertical displacement of solid Earth tides, the most prominent peak appears at 2 cpd. In contrast, at 1 cpd where the solid Earth tide spectrum exhibits its strongest peak (Figure 2d), no clear synchronization with RWE is observed. This discrepancy can be explained by the fact that both pressure and solid Earth tides share the 2 cpd harmonic. In this case, coherence does not reflect a direct causal link between solid Earth tides and RWE, but rather an indirect relationship mediated by the common periodicity present in pressure oscillations. We infer that atmospheric pressure is the dominant driver at 2 cpd, as only the MSC between atmospheric pressure and ellipticity displays a clear correlation at 1 cpd and across all harmonics (Figure 3c).

Figure 3d presents the MSC maps for all frequencies of the RWE function at station EHIG with respect to the three external drivers considered. Consistent with the spectrograms (Figure 3a–b), the E₁ and E₂ components exhibit the highest coherences with well-defined spectral peaks. In contrast, the targeted terdiurnal component (E₃) is only discernible at the highest



285



frequencies (> 45 Hz) in the coherence map with atmospheric pressure. These results motivate restricting the long-term analysis of the 3 cpd behavior to the 40–50 Hz frequency band.

Having established that the terdiurnal component (E₃) is restricted to the 40–50 Hz band, we next examine its long-term variability over 2007–2023. This analysis provides the basis for linking the 3 cpd oscillations to the effects of diffuse gas injections in the vadose zone. To do so, we assume that the coupling between atmospheric pressure and RWE variations can be described as a linear time-invariant system at that period. Under this assumption, the system response can be characterized by the complex transfer function

$$G(f) = \frac{P_{xy}(f)}{P_{xx}(f)} \tag{8}$$

The magnitude |G(f)| quantifies the gain of the RWE response relative to the input, while its phase expresses the frequency-dependent delay. As in the coherence analysis, all spectra were estimated with the Welch method using Hanning tapers.

Figure 4 shows the temporal evolution of the gain, phase lag, and MSC at the terdiurnal frequency (3 cpd) for the EHIG station from 2007 to 2023. These results were obtained using 15-day sliding windows with a 2-day step, and the resulting time series were smoothed with a 10-day moving median. In each window, the 3 cpd component was isolated by averaging the cross- and auto-spectra within a narrow frequency band centered at 3 cpd. The top panel displays the gain, deemed as well as the amplitude ratio between the RWE response and atmospheric pressure variations. The middle panel shows the corresponding phase lag expressed in hours, with positive values indicating that RWE is delayed with respect to pressure. The bottom panel presents the MSC, which quantifies the statistical stability of the coupling at this frequency.

The comparison between gain variations and CO₂ effluxes is challenging for several reasons. First, the two observables represent different physical scales: fluxes quantify the amount of gas released into the atmosphere, whereas RWE variations are most sensitive to changes within the upper meters of the subsurface. Specifically, in the 40–50 Hz band and using a reference velocity model constrained by tomographic studies of La Palma (e.g., Serrano et al., 2023; Cabrera-Pérez et al., 2023b), the RWE kernel is confined to depths shallower than ~5 m, with maximum sensitivity at ~2 m. A temporal delay between surface fluxes and subsurface RWE variations is therefore expected. Second, the CO₂ efflux dataset represents a spatial average over the entire volcanic edifice, while our RWE measurement reflects a point-specific response. Under a diffuse degassing regime, it is reasonable that individual sites exhibit their own local trends. Third, the temporal resolutions are markedly different: RWE gain was estimated every two days, whereas CO₂ effluxes are available as annual averages.



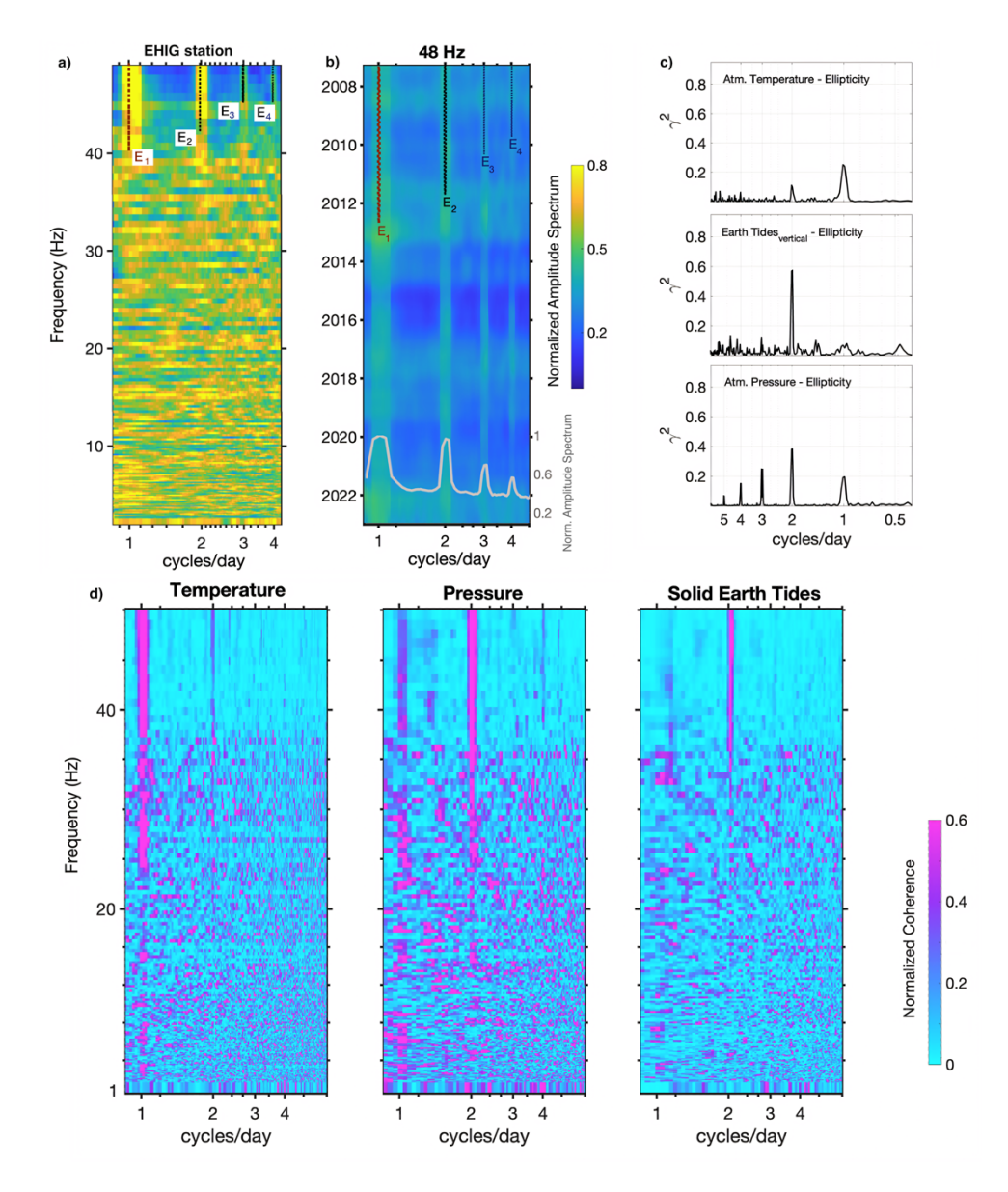


Figure 3. a) Normalized frequency-period Fourier spectrogram of the RWE series during 2010 (frequency range 1–50 Hz) at EHIG station. Sliding windows of 30 days with 50% overlap were applied. Distinct spectral peaks at 1, 2, 3, and 4 cycles per day are observed and labeled as E₁–E₄. b) Time-frequency Fourier spectrogram of the 48 Hz RWE series (2007–2023), showing the persistence of the four subdaily components throughout the record. The overlaid gray curve at the bottom displays the time-stacked normalized average spectrum over the entire study period. c) Magnitude-squared coherence between 48 Hz ellipticity and external drivers: atmospheric temperature (top), vertical component of displacement from solid Earth tides (middle), and atmospheric pressure (bottom). d) Frequency-period MSC maps between RWE and the three drivers for the period 2007–2010. Sliding windows of 30 days with 50% overlap were used. For visualization, coherence at each RWE frequency was normalized by its maximum.



310

315

320

325



Despite these differences in scale, resolution, and sensitivity, both curves display broadly consistent long-term trends, suggesting a moderate agreement between the two observations (see Figure A2 in Appendix). As reasoned in Section 3.1, an increase in gas concentration reduces the effective gas compressibility and enhances the hydraulic diffusivity. In the transfer function analysis, this process is expected to manifest as an increase in gain, reflecting the more efficient transmission of pressure oscillations into the subsurface.

Between 2015 and 2017 we observe a marked increase in coherence, accompanied by a rise in gain that could indicate a stronger degassing episode in this area (Figure 4). Unfortunately, no direct records of gas emissions are available for this period to validate this interpretation. Over the entire study period, the phase lag displays a clear seasonal variability. Soil moisture and precipitation are known to influence gas transport by attenuating barometric pumping (Forde et al., 2019). Consistently, comparison of the phase lag results with the rainfall pattern for La Palma suggests a possible influence of precipitation. The seasonal oscillations in phase show a moderate alignment with the island's annual precipitation cycle, which may reflect transient reductions in diffusivity caused by water infiltration into the vadose zone. This observation departs from our initial assumption of a purely gas-filled vadose zone and underscores the role of hydrological processes in modulating the pressure response.

No sustained trend in gain, coherence, or phase that could be interpreted as a precursor signal to the 2021 eruption is observed at this station, suggesting that the eruptive episode did not correspond to the most intense period of diffuse degassing within its long-term record. Only a slight increase in coherence during the eruption episode and in early 2021 is remarkable, together with a disruption of the purely annual phase seasonality observed in mid-2020 and mid-2021, when the phase lag tended to approach zero (Anomalies marked in Figure 4). As these phase lag perturbations are not accompanied by a corresponding increase in gain, we interpret them as changes in the hydrological state of the vadose zone, most likely related to variations in soil moisture or permeability of the soil, rather than as evidence of enhanced gas injections.

Having characterized the long-term behavior at EHIG for the 3 cpd, we next examined whether similar signatures could be detected at stations located nearer to the eruption site. For this purpose, we analyzed the TBT and EXILP stations (Figure 1), whose records cover 2019–2023 and encompass the pre-eruptive, eruptive, and post-eruptive periods. Given that station EXILP is an accelerometer, its records were first converted to velocity using the instrument response. In addition, because its sampling rate is 200 Hz, our analysis focused on the 50–100 Hz frequency band, in contrast to the 1–50 Hz band used at the other two stations. This choice is not only consistent with the data resolution, but also physically meaningful: higher frequencies provide sensitivity to shallower depths. As shown by the sensitivity kernels (Figure A3 in Appendix), the 40–50 Hz band is maximally sensitive to depths of about 2 m, while sensitivity shifts to ~1 m in the 90–100 Hz range. Figure 5a shows the amplitude spectrum for EXILP within this frequency range. At this station the four spectral peaks identified at EHIG (E₁–E₄) are also present. Figure 5b displays the temporal evolution of gain, phase, and coherence in the 90–100 Hz





band. No systematic trend or increase in coherence is observed prior to the eruption, although a rise in gain is evident at the onset of the eruptive episode.

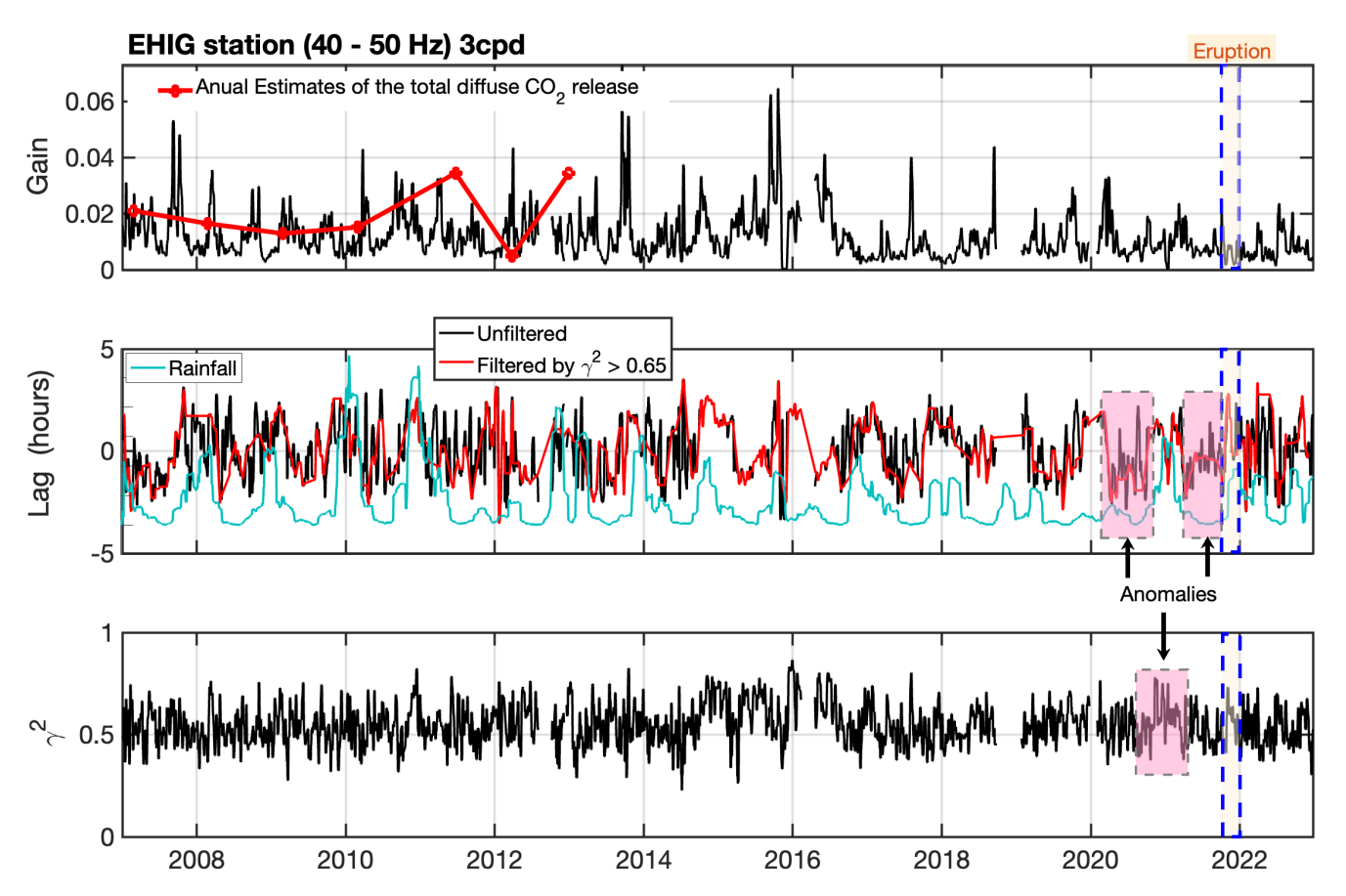


Figure 4. a) Gain |G(3 cpd)| at EHIG station (40–50 Hz band, 2007–2023) shown in black, with annual estimates of the total diffuse CO₂ release overlaid in red. b) Phase lag at 3 cpd (black) together with the same series filtered by magnitude-squared coherence $\gamma^2 > 0.65$ (red), and rainfall shown in cyan. c) Magnitude-squared coherence γ^2 at 3 cpd. All three metrics were computed in sliding windows of 15 days with 13-day overlap (2-day step) on time series sampled at 2-hour intervals, and displayed as 5-point moving medians. The dashed blue rectangle marks the 2021 eruption. Shaded pink boxes highlight anomalous intervals discussed in the text.



365



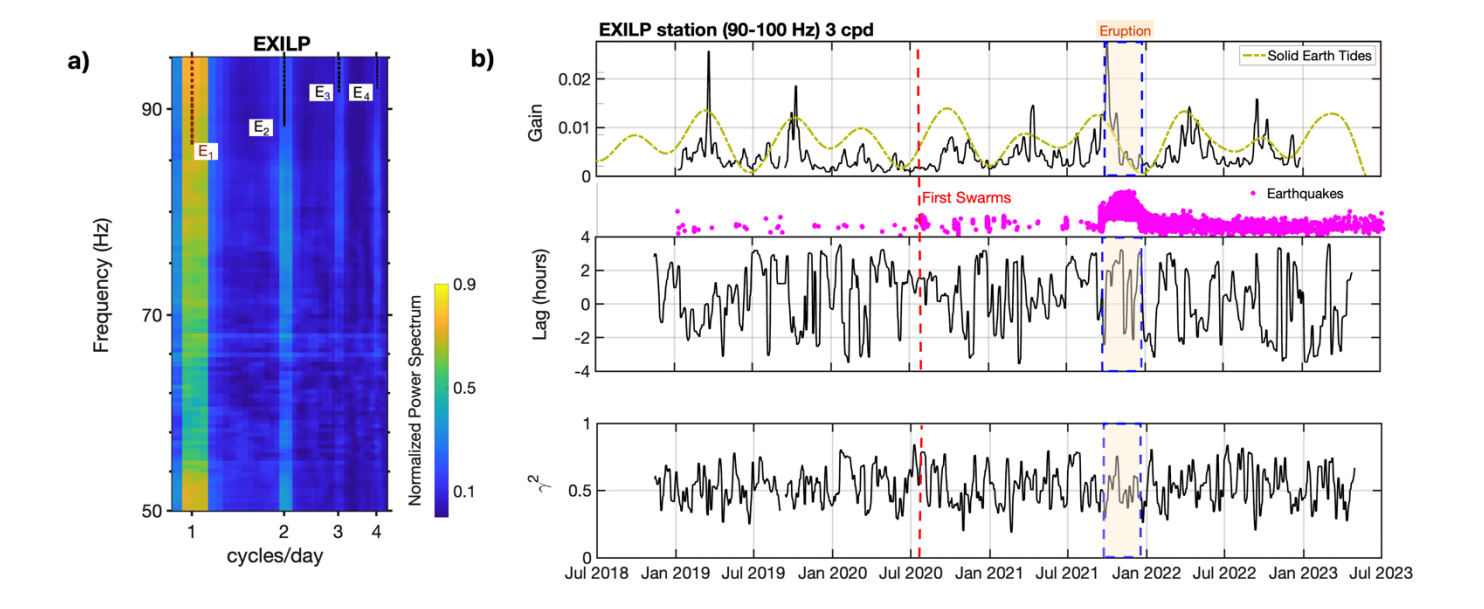


Figure 5. a) Normalized frequency-period Fourier spectrogram of the RWE series during 2021 (frequency range 50–100 Hz) at EXILP station. Sliding windows of 30 days with 50% overlap were applied. Distinct spectral peaks at 1, 2, 3, and 4 cycles per day are observed and labeled as E₁-E₄. b) Transfer-function results at 3 cpd for the 90–100 Hz band at EXILP station (2019–2023): (top) Gain |G (3 cpd)| shown in black, with the vertical solid Earth tide displacement (dashed green) computed with the Python package pysolid (Yunjun et al., 2022) and bandpass filtered between 100 and 300 days. Magenta dots represent individual earthquakes, plotted according to their occurrence time (x-axis) and magnitude (m_{bLg}, y-axis). The largest event reached m_{bLg} 5.1. (middle) Phase lag at 3 cpd. (bottom) Magnitude-squared coherence γ² at 3 cpd. All three metrics were computed in sliding windows of 15 days with 13-day overlap (2-day step) on time series sampled at 2-hour intervals, and displayed as 5-point moving medians. The dashed blue rectangle marks the 2021 eruption.

An additional and particularly noteworthy finding is the presence of a clear semi-annual cycle in the gain, consistently observed throughout the study period (Figure 5b). When examining the gain at the three analyzed stations, semi-annual cycles are also apparent (Figures 4, 5 and 6). At EHIG, for example, during the low CO₂ emission period (2007–2010) the cycle is clearly expressed (Figure 4), and at TBT a semi-annual modulation emerges with peaks in March and September and minima in July and December (Figure 6b), a seasonal pattern that is synchronized across the three stations. Although environmental variables such as volumetric soil water content, wind, or even atmospheric pressure can also exhibit semi-annual variability, none of them display a pattern as regular and well-defined as the solid Earth tides. The latter provide an excellent agreement with the cycles observed at the three stations, supporting our hypothesis that the detected semi-annual modulation reflects the influence of solid tidal forcing



375

380

385



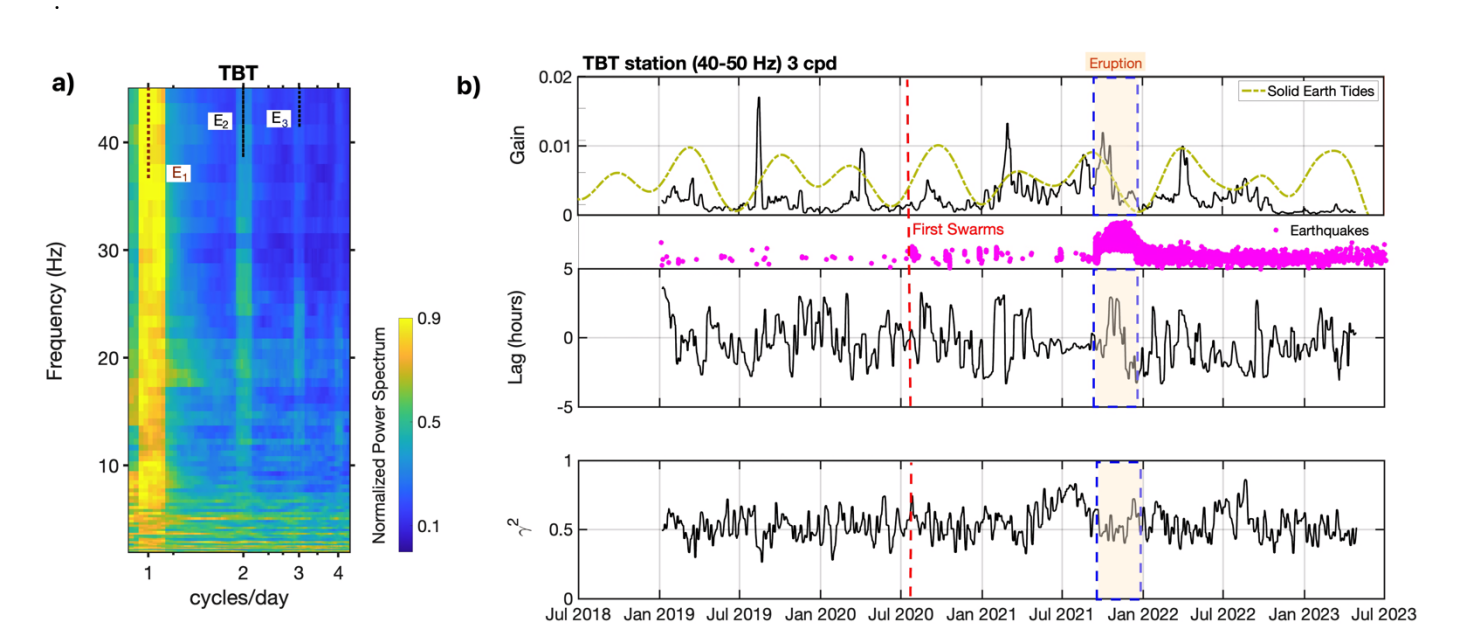


Figure 6. a) Normalized frequency-period Fourier spectrogram of the RWE series during 2021 (frequency range 1–50 Hz) at TBT station. Sliding windows of 30 days with 50% overlap were applied. Distinct spectral peaks at 1, 2 and 3 cycles per day are observed and labeled as E₁-E₃. b) Transfer-function results at 3 cpd for the 40–50 Hz band at TBT station (2019–2023): (top) Gain |G (3 cpd)| shown in black, with the vertical solid Earth tide displacement (dashed green) computed with the Python package pysolid (Yunjun et al., 2022) and bandpass filtered between 100 and 300 days. Magenta dots represent individual earthquakes, plotted according to their occurrence time (x-axis) and magnitude (m_{bLg}, y-axis). The largest event reached m_{bLg} 5.1. (middle) Phase lag at 3 cpd. (bottom) Magnitude-squared coherence γ² at 3 cpd. All three metrics were computed in sliding windows of 15 days with 13-day overlap (2-day step) on time series sampled at 2-hour intervals, and displayed as 5-point moving medians. The dashed blue rectangle marks the 2021 eruption.

This semi-annual modulation can be physically explained by the response of the fractured medium to solid Earth tides. At the peaks of the vertical tidal component, fractures are expected to open, leading to an increase in the effective permeability of the medium. As described by Equations (2) – (4), an increase in permeability directly translates into higher diffusivity and thus a more efficient propagation of the barometric pressure wave. Consequently, earth tidal peaks are expressed as gain maxima, in agreement with the observed cycles at the three stations (Figures 4a-5b-6b). This result highlights not only the potential of our approach to monitor subsurface gas accumulation, but also its ability to detect permeability changes driven by tidal forcing. In settings where degassing or significant gas fluxes from the critical zone are not expected, analyzing the 3 cpd cycle and its response to solid Earth tides provides a novel tool to probe short-term variations in subsurface permeability. We therefore propose that tidal modulation of barometric pumping can serve as a powerful diagnostic for permeability changes, with applications extending well beyond volcanic environments.



390

395

405

410

415



Although the semi-annual modulation provides a common background signal at all stations, its expression depends on the degassing regime. At EHIG, for example, the cycle is most clearly observed during periods of low CO₂ emission and becomes less evident when degassing intensifies (Figure 4). TBT, however, shows an additional feature: a marked increase in coherence together with a stabilization of the lag prior to the eruption (Figure 6), pointing to localized changes in permeability or gas flux that were not equally expressed elsewhere. Notably, this anomaly would not be apparent if one considered gain alone, since the initial increase in coherence coincided with a decrease in the vertical solid Earth tide, corresponding to a scenario of fracture compression. Under such conditions, even if gas injection occurred, the simultaneous closure of fractures would dampen the gain response. Coherence and lag therefore provide complementary information, revealing subsurface changes that are not fully captured by gain. While we lack direct measurements of gas flux to validate this observation, our interpretation is that the increase in coherence and stabilization of the lag at TBT reflects subsurface gas accumulation and possibly anomalous efflux to the atmosphere about six months before the eruption.

This distinctive behavior at TBT can be explained by its structural and hydrogeological setting. The station is located within 400 a highly fractured zone affected by abundant vertical dike intrusions and intersected by water wells and galleries, which together enhance vertical permeability and pressure transmission. Such structural discontinuities likely provide preferential pathways for gas ascent from the underlying hydrothermal system, amplifying the coupling between barometric pumping and subsurface gas accumulation. In contrast, stations located in less fractured domains or outside the main hydrothermal influence, such as Taburiente Caldera (Figure 1), lack this level of connectivity and therefore do not record the same precursor signal. To further verify that the observed anomaly at TBT reflects atmospheric forcing rather than random fluctuations or other mechanisms, we examined the frequency dependence of the coherence (γ^2) and the standard deviation of the lag (σ_{Lag}) around the terdiurnal cycle (Figure 7). The results show that the enhanced coherence and reduced lag variability preceding the eruption are consistently observed between 2.9 and 3.1 cpd, with the strongest signal at 3.0 cpd. This narrowband expression supports the interpretation that the anomaly is linked to barometric pumping and thus constitutes a genuine precursor signal.

In addition, shallow geology plays also an important control on the observed tidal response. Among the three stations, the 6hour cycle (E₄) is notably weak at TBT (Figure 4a). This can be explained by its location on alluvial and colluvial deposits in the Barranco de las Angustias, where heterogeneous grain-size distribution and lower effective permeability likely dampen the higher-frequency component of pressure diffusion. In contrast, EHIG and EXILP, situated both on young basaltic flows, overlie more permeable substrates that facilitate the transmission of short-period cycles, resulting in a clearer E₄ expression (Figures 3 a-b, 4a).





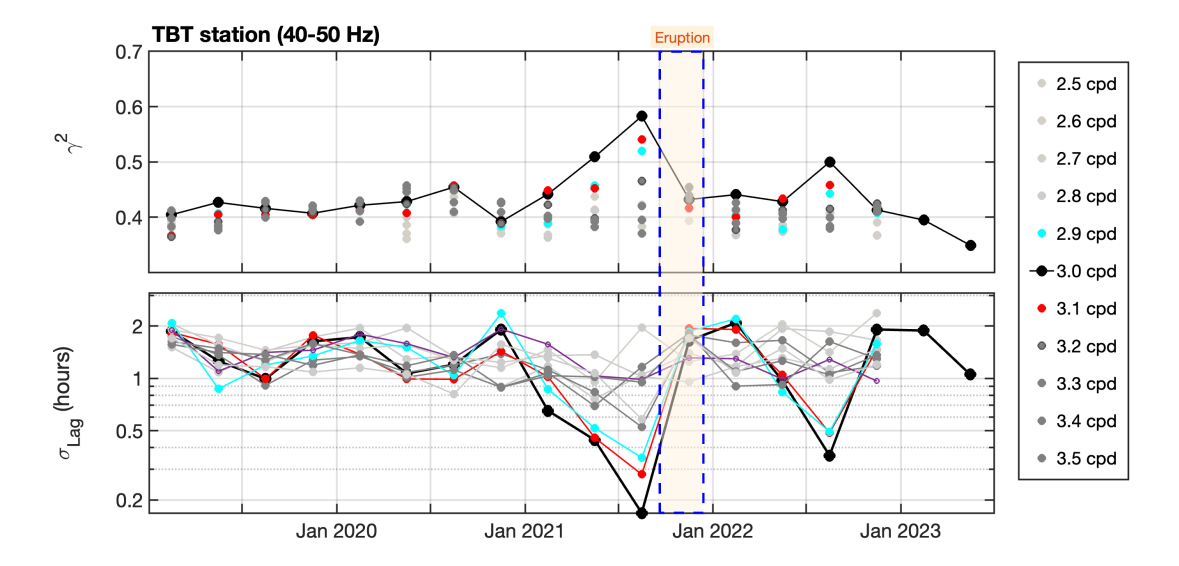


Figure 7. Frequency dependence of coherence (top) and the standard deviation of the lag (bottom) at TBT station (40–50 Hz band) for frequencies between 2.5 and 3.5 cpd, computed using 3-month averaging windows based on transfer function analysis (Figure 6). A consistent increase in coherence and reduction in lag variability is observed between 2.9 and 3.1 cpd, most pronounced at 3.0 cpd, during the months preceding the 2021 eruption (blue dashed rectangle).

The clear expression of the 3 cpd cycle in our data greatly facilitated both the analysis and interpretation of the results. Isolating the barometric driver is critical because RWE alone does not unambiguously distinguish between changes in Vs and 425 V_P. Based on our previous reasoning in Section 3.2, pressure-induced velocity oscillations are expected to primarily affect V_P when gas is injected into the pore space. Thus, by targeting a spectral band where the barometric forcing dominates, we reduce the ambiguity in interpreting RWE changes and strengthen the case for attributing them to variations in V_P and therefore to gas injections, rather than to changes in Vs. However, this component may not always be observable in other contexts. In such cases, alternative strategies could focus on more energetic pressure cycles, such as the 2 cpd barometric 430 tide. This option is complicated by the frequency overlap of this atmospheric harmonic with the solar semidiurnal solid Earth tide (S₂), the semidiurnal ocean tide, and the nearby lunar constituent M₂. In hydrogeology, this difficulty is commonly addressed through the concept of barometric efficiency and its frequency-domain formulations (e.g., Acworth et al., 2016; Valois et al., 2022), which exploit the spectral relationship between S2 and M2 to separate atmospheric and solid Earth contributions. Nevertheless, because the lunar semidiurnal constituent (M2) is not clearly expressed in our observations for 435 La Palma, such approaches cannot be straightforwardly applied here to investigate degassing processes using the 2 cpd cycle.

Taken together, our results demonstrate that RWE provides a sensitive tool to track both gas injections and permeability changes in the upper vadose zone. The comparison with CO₂ efflux data shows a consistent trend with the gain observed at EHIG, despite differences in spatial scale and temporal resolution (Figure 4). The robust semi-annual modulation observed





across stations can be explained by the tidal control of fracture permeability through solid Earth tides, while site-specific anomalies reveal how additional processes shape the response. At EHIG, the seasonal variability of phase is consistent with hydrological control, most likely linked to soil moisture and rainfall (Figure 4). In contrast, at TBT, the pre-eruptive increase in coherence and stabilization of lag point to subsurface gas accumulation and possibly anomalous efflux several months before the 2021 eruption (Figure 6). This highlights the value of jointly analyzing gain, phase, and coherence, since they provide complementary constraints on the physical processes controlling the pressure response. Through a denser seismic network, this approach could provide more continuous observations, improve our understanding of volcanic degassing processes, and enhance hazard mitigation by enabling remote monitoring without the need to deploy personnel in hazardous areas. Overall, our findings indicate that the 3 cpd component constitutes a reliable diagnostic of pressure-driven processes in the shallow subsurface, with the potential to identify subtle diffusivity changes.

5. Conclusions

This study demonstrates for the first time that RWE from ambient noise can be used to track ground variability induced by tidal forcing. Our analysis focuses mainly on air-pressure tides and shows that RWE provides a robust measure of seismic velocity changes, which we interpret as proxies for diffuse volcanic degassing and transient gas transport. Unlike conventional seismic interferometry, which fails during eruptive tremor, RWE remains effective in high-noise volcanic environments. Our results establish a clear link between subsurface pressure oscillations and gas transport, suggesting that the analysis of RWE variations at subdaily tidal cycles provides a novel pathway to monitor permeability changes and degassing in volcanic systems, with direct implications for hazard assessment and early warning. In addition, although our analysis was primarily designed to investigate the evolution of the 3 cpd cycle driven by atmospheric forcing, we uncovered a clear interplay with the semi-annual modulation imposed by solid Earth tides, demonstrating the influence of Earth tidal forcing in controlling fracture permeability.

The pre-eruptive and eruptive records of the three stations reveal distinct but complementary patterns. At EHIG, only a slight increase in coherence is observed during the eruption, together with a disruption of the annual phase seasonality in mid-2020 and mid-2021, when the phase lag tended to approach zero. At EXILP, the highest gain of the entire series coincides with the onset of the eruption, but no significant precursory anomalies are detected. In contrast, TBT exhibits clear pre-eruptive signals, including a marked increase in coherence, stabilization of the lag, and a progressive rise in gain starting about six months before the eruption. This distinct precursor at TBT likely reflects its location in a highly fractured zone, which enhances vertical connectivity and gas-driven responses to atmospheric forcing.

While this study focuses on Cumbre Vieja, the method is applicable to other volcanic systems, geothermal reservoirs, and CO₂ storage sites, where monitoring pressure-driven gas transport is essential for stability and leakage detection.





Code availability

The link to the source routines for the degree of polarization method (Schimmel & Gallart, 2003) can be found in Berbellini et al. (2019).

Data availability

The seismic data used in this study are publicly available through FDSN data services for the ES network and the 9A networks (Instituto Geografico Nacional, 1999; Walter et al. 2021). The atmospheric data were obtained from the ERA5 database (Copernicus Climate Change Service, 2018).

Author contributions

HS and MS: investigation. HS and MS: conceptualization. HS: data preparation. HS and MS: methodology. HS and MS: software. HS and MS: formal analysis. HS: writing (original draft). HS and MS: writing (review and editing). HS: visualization. MS: supervision. HS: validation.

480 Competing interests

The authors have no relevant competitive or financial interests to disclose.

Acknowledgements

This work has received funding from the AGEMERA project, financed by the European Union's Horizon Europe research and innovation programme under grant agreement N° 101058178. During the preparation of this work, the firt author used ChatGPT, an AI language model developed by OpenAI, in order to assist with drafting and refining the manuscript. After using this tool, the authors reviewed and edited the content as needed and take full responsibility for the content of the publication.

490

475





References

500

505

510

- Acworth, R.I., Halloran, L.J.S., Rau, G.C., Cuthbert, M.O., Bernardi, T.L., 2016. An objective frequency domain method for quantifying confined aquifer compressible storage using Earth and atmospheric tides. Geophysical Research Letters 43. https://doi.org/10.1002/2016GL071328
- Auer, L.H., Rosenberg, N.D., Birdsell, K.H., Whitney, E.M., 1996. The effects of barometric pumping on contaminant transport. Journal of Contaminant Hydrology 24, 145–166. https://doi.org/10.1016/S0169-7722(96)00010-1
- Berbellini, A., Schimmel, M., Ferreira, A.M., Morelli, A., 2019. Constraining *S* -wave velocity using Rayleigh wave ellipticity from polarization analysis of seismic noise. Geophysical Journal International 216, 1817–1830. https://doi.org/10.1093/gji/ggy512
- Brace, W.F., Walsh, J.B., Frangos, W.T., 1968. Permeability of granite under high pressure. J. Geophys. Res. 73, 2225–2236. https://doi.org/10.1029/JB073i006p02225
- Cabrera-Pérez, I., D'Auria, L., Soubestre, J., Przeor, M., Barrancos, J., García-Hernández, R., Ibáñez, J.M., Koulakov, I., Van Dorth, D.M., Ortega, V., Padilla, G.D., Sagiya, T., Pérez, N., 2023a. Spatio-temporal velocity variations observed during the pre-eruptive episode of La Palma 2021 eruption inferred from ambient noise interferometry. Sci Rep 13, 12039. https://doi.org/10.1038/s41598-023-39237-9
- Cabrera-Pérez, I., Soubestre, J., D'Auria, L., Barrancos, J., Martín-Lorenzo, A., Van Dorth, D.M., Padilla, G.D., Przeor, M., Pérez, N.M., 2023b. Geothermal and structural features of La Palma island (Canary Islands) imaged by ambient noise tomography. Sci Rep 13, 12892. https://doi.org/10.1038/s41598-023-39910-z
- Carracedo, J.C., Badiola, E.R., Guillou, H., De La Nuez, J., Pérez Torrado, F.J., 2001. Geology and volcanology of La Palma and El Hierro, Western Canaries. Estud. geol. 57, 175–273. https://doi.org/10.3989/egeol.01575-6134
 - Carvalho, J., Silveira, G., Mendes, V.B., Schimmel, M., Antón, R., 2024. Insights into fluid migration during the 2021 La Palma eruption using seismic noise interferometry. Front. Earth Sci. 12, 1298472. https://doi.org/10.3389/feart.2024.1298472
- Cercato, M., 2018. Sensitivity of Rayleigh wave ellipticity and implications for surface wave inversion. Geophysical Journal International 213, 489–510. https://doi.org/10.1093/gji/ggx558
 - Conte, E., Cosentini, R.M., Troncone, A., 2009. Shear and dilatational wave velocities for unsaturated soils. Soil Dynamics and Earthquake Engineering 29, 946–952. https://doi.org/10.1016/j.soildyn.2008.11.001
 - Copernicus. ERA5 Hourly Data on Single Levels from 1979 to Present. Available online: https://cds.climate.copernicus.eu/cdsapp#!/dataset/reanalysis-era5-single-levels?tab=overview, n.d.
 - Dirección General de Costas, 2004. Study of tides and hydrographic zero. Ecocartographic study of the coast of La Palma Island (No. Technical Report P02202_ATLP_cero_v04). Ministerio de Medio Ambiente, Dirección General de Costas, Madrid, Spain.



550



- Epiard, M., Avard, G., De Moor, J.M., Martínez Cruz, M., Barrantes Castillo, G., Bakkar, H., 2017. Relationship between

 Diffuse CO2 Degassing and Volcanic Activity. Case Study of the Poás, Irazú, and Turrialba Volcanoes, Costa Rica.

 Front. Earth Sci. 5, 71. https://doi.org/10.3389/feart.2017.00071
 - Forde, O.N., Cahill, A.G., Beckie, R.D., Mayer, K.U., 2019. Barometric-pumping controls fugitive gas emissions from a vadose zone natural gas release. Sci Rep 9, 14080. https://doi.org/10.1038/s41598-019-50426-3
- Galone, L., Panzera, F., Colica, E., Fucks, E., Carol, E., Cellone, F., Rivero, L., Agius, M.R., D'Amico, S., 2024. A Seismic Monitoring Tool for Tidal-Forced Aquifer Level Changes in the Río de la Plata Coastal Plain, Argentina. Sustainability 16, 1432. https://doi.org/10.3390/su16041432
 - García-Gil, A., Jimenez, J., Marazuela, M.Á., Baquedano, C., Martínez-León, J., Cruz-Pérez, N., Laspidou, C., Santamarta, J.C., 2023. Effects of the 2021 La Palma volcanic eruption on groundwater resources (part I): Hydraulic impacts. Groundwater for Sustainable Development 23, 100989. https://doi.org/10.1016/j.gsd.2023.100989
- Gomell, A., Austin, D., Ohms, M., Pflitsch, A., 2021. Air pressure propagation through Wind Cave and Jewel Cave: How do pressure waves travel through barometric caves? IJS 50, 263–273. https://doi.org/10.5038/1827-806X.50.3.2393
 - Haghshenas, E., Bard, P.-Y., Theodulidis, N., SESAME WP04 Team, 2008. Empirical evaluation of microtremor H/V spectral ratio. Bull Earthquake Eng 6, 75–108. https://doi.org/10.1007/s10518-007-9058-x
- Hanks, R.J., Woodruff, N.P., n.d. Influence of wind on water vapor transfer through soil, gravel, and straw mulches. Soil Science 86, 160–164.
 - Hernández, P.A., Notsu, K., Salazar, J.M., Mori, T., Natale, G., Okada, H., Virgili, G., Shimoike, Y., Sato, M., Pérez, N.M., 2001. Carbon Dioxide Degassing by Advective Flow from Usu Volcano, Japan. Science 292, 83–86. https://doi.org/10.1126/science.1058450
 - Jiao, J.J., Li, H., 2004. Breathing of coastal vadose zone induced by sea level fluctuations. Geophysical Research Letters 31, 2004GL019572. https://doi.org/10.1029/2004GL019572
 - Kramer, R., Lu, Y., Bokelmann, G., 2023. Interaction of Air Pressure and Groundwater as Main Cause of Sub-Daily Relative Seismic Velocity Changes. Geophysical Research Letters 50, e2022GL101298. https://doi.org/10.1029/2022GL101298
- Kuang, X., Jiao, J.J., Li, H., 2013. Review on airflow in unsaturated zones induced by natural forcings: Subsurface Airflow Induced By Natural Forcings. Water Resour. Res. 49, 6137–6165. https://doi.org/10.1002/wrcr.20416
 - Lin, W., 1977. Compressible fluid flow through rocks of variable permeability Rep. UCRL-52304, 15.
 - Luu, K., 2021. disba: Numba-accelerated computation of surface wave dispersion. https://doi.org/10.5281/ZENODO.5775195
 - Maupin, V., 2017. 3-D sensitivity kernels of the Rayleigh wave ellipticity. Geophysical Journal International 211, 107–119. https://doi.org/10.1093/gji/ggx294





- Merrit, M., 2004. Estimating hydraulic properties of the Floridan Aquifer System by analysis of earth-tide, ocean-tide, and barometric effects, Collier and Hendry Counties, Florida (No. 2003–4267). U.S. Geological Survey. https://doi.org/10.3133/wri034267
- Mezcua, J., Rueda, J., 2024. Seismic Velocity Variations Observed Prior to the La Palma Volcano Eruption on 19

 September 2021, in Cumbre Vieja, Canary Islands (Spain). The Seismic Record 4, 11–20.

 https://doi.org/10.1785/0320230048
 - Nilson, R.H., Peterson, E.W., Lie, K.H., Burkhard, N.R., Hearst, J.R., 1991. Atmospheric pumping: A mechanism causing vertical transport of contaminated gases through fractured permeable media. J. Geophys. Res. 96, 21933–21948. https://doi.org/10.1029/91JB01836
- Padrón, E., Pérez, N.M., Hernández, P.A., Sumino, H., Melián, G., Barrancos, J., Nolasco, D., Padilla, G., 2012. Helium emission at Cumbre Vieja volcano, La Palma, Canary Islands. Chemical Geology 312–313, 138–147. https://doi.org/10.1016/j.chemgeo.2012.04.018
 - Padrón, E., Pérez, N.M., Rodríguez, F., Melián, G., Hernández, P.A., Sumino, H., Padilla, G., Barrancos, J., Dionis, S., Notsu, K., Calvo, D., 2015. Dynamics of diffuse carbon dioxide emissions from Cumbre Vieja volcano, La Palma, Canary Islands. Bull Volcanol 77, 28. https://doi.org/10.1007/s00445-015-0914-2
 - Pérez, N.M., Melián, G.V., Hernández, P.A., Padrón, E., Padilla, G.D., Baldago, Ma.C., Barrancos, J., Rodríguez, F., Asensio-Ramos, M., Alonso, M., Arcilla, C., Lagmay, A.M., 2022. Diffuse CO2 degassing precursors of the January 2020 eruption of Taal volcano, Philippines. Sci Rep 12, 19091. https://doi.org/10.1038/s41598-022-22066-7
- Poncela, R., Santamarta, J.C., García-Gil, A., Cruz-Pérez, N., Skupien, E., García-Barba, J., 2022. Hydrogeological characterization of heterogeneous volcanic aquifers in the Canary Islands using recession analysis of deep water gallery discharge. Journal of Hydrology 610, 127975. https://doi.org/10.1016/j.jhydrol.2022.127975
 - Robinson, E.S., Bell, R.T., 1971. Tides in confined well-aquifer systems. J. Geophys. Res. 76, 1857–1869. https://doi.org/10.1029/JB076i008p01857
- Sánchez-Pastor, P., Obermann, A., Schimmel, M., 2018. Detecting and Locating Precursory Signals During the 2011 El

 Hierro, Canary Islands, Submarine Eruption. Geophysical Research Letters 45.

 https://doi.org/10.1029/2018GL079550
 - Sánchez-Pastor, P., Wu, S.-M., Hokstad, K., Kristjánsson, B., Drouin, V., Ducrocq, C., Gunnarsson, G., Rinaldi, A., Wiemer, S., Obermann, A., 2023. Steam caps in geothermal reservoirs can be monitored using seismic noise interferometry. Commun Earth Environ 4, 453. https://doi.org/10.1038/s43247-023-01122-8
- Santana De León, J.M., Melián, G.V., Rodríguez, C., Cervigón-Tomico, G., Ortega, V., Martínez Van Dorth, D., Cabrera-Pérez, I., Cordero, M., Przeor, M., Silva, R.F.F., Matos, S.B.D., Baldoni, E., Ramalho, M.M.P., Viveiros, F., Calvo, D., Pérez, N.M., 2022. Long-term variations of diffuse CO2 at Cumbre Vieja volcano, La Palma, Canary Islands. https://doi.org/10.5194/egusphere-egu22-8773





- Sato, K., 2006. Monitoring the underground migration of sequestered carbon dioxide using Earth tides. Energy Conversion and Management 47, 2414–2423. https://doi.org/10.1016/j.enconman.2005.11.005
 - Schimmel, M., Gallart, J., 2003. The use of instantaneous polarization attributes for seismic signal detection and image enhancement. Geophysical Journal International 155, 653–668. https://doi.org/10.1046/j.1365-246X.2003.02077.x
 - Seivane, H., García-Jerez, A., Navarro, M., Molina, L., Navarro-Martínez, F., 2022. On the use of the microtremor HVSR for tracking velocity changes: a case study in Campo de Dalías basin (SE Spain). Geophysical Journal International 230, 542–564. https://doi.org/10.1093/gji/ggac064
 - Seivane, H., Schimmel, M., Martí, D., Sánchez-Pastor, P., 2024. Rayleigh wave ellipticity from ambient noise: A practical method for monitoring seismic velocity variations in the near-surface. Engineering Geology 343, 107768. https://doi.org/10.1016/j.enggeo.2024.107768
- Serrano, I., Dengra, M.A., Almendros, F.J., Torcal, F., Zhao, D., 2023. Seismic anisotropy tomography beneath La Palma in the Canary Islands, Spain. Journal of Volcanology and Geothermal Research 441, 107870. https://doi.org/10.1016/j.jvolgeores.2023.107870
 - Troll, V.R., Carracedo, J.C., 2016. The Geology of La Palma, in: The Geology of the Canary Islands. Elsevier, pp. 101–180. https://doi.org/10.1016/B978-0-12-809663-5.00003-7
- Valois, R., Rau, G.C., Vouillamoz, J., Derode, B., 2022. Estimating Hydraulic Properties of the Shallow Subsurface Using the Groundwater Response to Earth and Atmospheric Tides: A Comparison With Pumping Tests. Water Resources Research 58, e2021WR031666. https://doi.org/10.1029/2021WR031666
 - Vassallo, M., Cultrera, G., Di Giulio, G., Cara, F., Milana, G., 2022. Peak Frequency Changes From HV Spectral Ratios in Central Italy: Effects of Strong Motions and Seasonality Over 12 Years of Observations. JGR Solid Earth 127, e2021JB023848. https://doi.org/10.1029/2021JB023848
- Viveiros, F., Silva, C., 2024. Hazardous volcanic CO2 diffuse degassing areas A systematic review on environmental impacts, health, and mitigation strategies. iScience 27, 110990. https://doi.org/10.1016/j.isci.2024.110990
 - Walter, T., Dahm, T., Cesca, S., Valenzuela-Malebran, C., Milkereit, C., Richter, N., Shevshenko, A., Vollmer, D., Kriegerowski, M., 2021. HART-La Palma volcanic eruption. https://doi.org/10.14470/4N7576350874
- Wang, C.-Y., Manga, M., 2021. Response to Tides, Barometric Pressure and Seismic Waves, in: Water and Earthquakes,

 Lecture Notes in Earth System Sciences. Springer International Publishing, Cham, pp. 83–153.

 https://doi.org/10.1007/978-3-030-64308-9 5
 - Welch, P., 1967. The use of fast Fourier transform for the estimation of power spectra: A method based on time averaging over short, modified periodograms. IEEE Transactions on audio and electroacoustics 15, 70–73.
- Yunjun, Z., Fattahi, H., Pi, X., Rosen, P., Aoki, Y., 2022. PySolid: A Python wrapper for solid Earth tides. GitHub repository.
 - Zimmerman, R.W., 2018. The Imperial College Lectures in Petroleum Engineering: Volume 5: Fluid Flow in Porous Media. WORLD SCIENTIFIC (EUROPE). https://doi.org/10.1142/q0146





Appendix

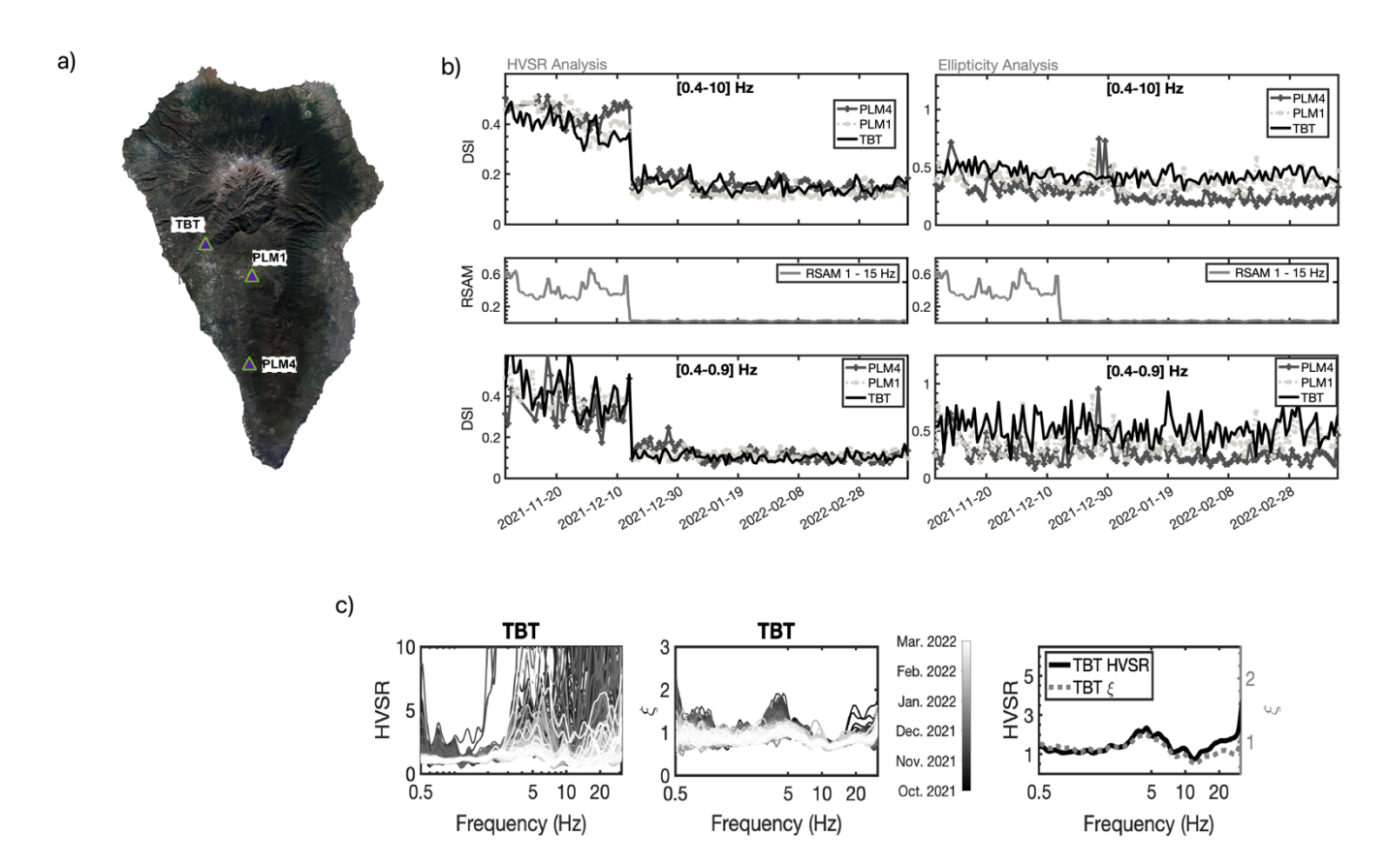


Figure A1. Comparison of the Dissimilarity Index (DSI) evolution from HVSNR analysis (left panels) and Rayleigh wave ellipticity (ξ) analysis (right panels) at three seismic stations (PLM4, PLM1, from network 9A, GFZ Data Services; and TBT, from network ES, IGN Red Sísmica Nacional) during and after the 2021 La Palma eruption. (a) Location of the three seismic stations used in this comparison. (b) The top and bottom panels show the temporal evolution of the DSI for two frequency bands: 0.4–10 Hz (upper) and 0.4–0.9 Hz (lower). The central panels display the Real-time Seismic Amplitude Measurement (RSAM, 1–15 Hz) as a proxy for tremor amplitude. A sharp drop in the DSI from the HVSNR analysis is observed following the eruption cessation, coinciding with the tremor amplitude decrease. In contrast, the DSI derived from ellipticity analysis remains stable, demonstrating its robustness against tremor-related amplitude variations. (c) Comparison of Ellipticity (center) and HVSNR curves (left) for TBT station, with colors representing different time periods from October 2021 to March 2022. The right panel compares the median HVSNR and Ellipticity curves for TBT station. The stabilization of the median around the most recurrent values explains the similarity between the curves in the lower-right panel, as the analyzed period contains more data after the eruption cessation than during the eruption.





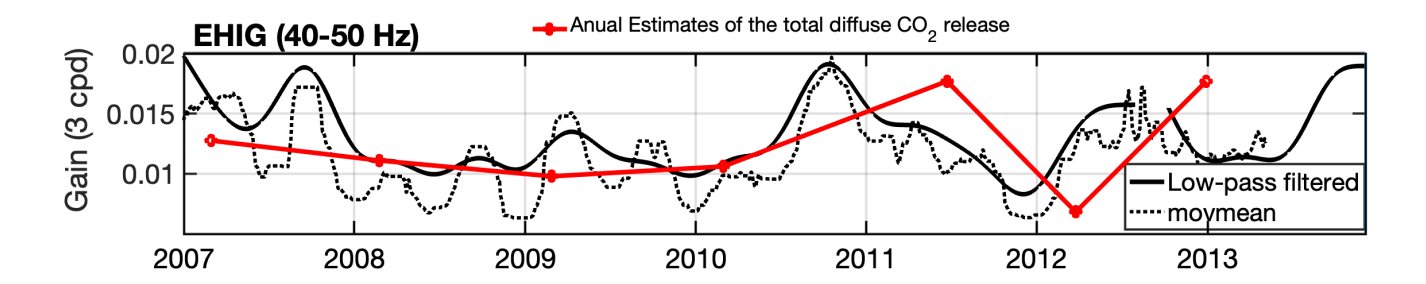


Figure A2. Gain |G (3 cpd)| at EHIG station (40–50 Hz band, 2007–2013), compared with annual estimates of the total diffuse CO₂ release overlaid in red. The black solid line shows the series low-pass filtered with a 240-day cutoff, while the dashed line indicates the 240-day moving-average mean.

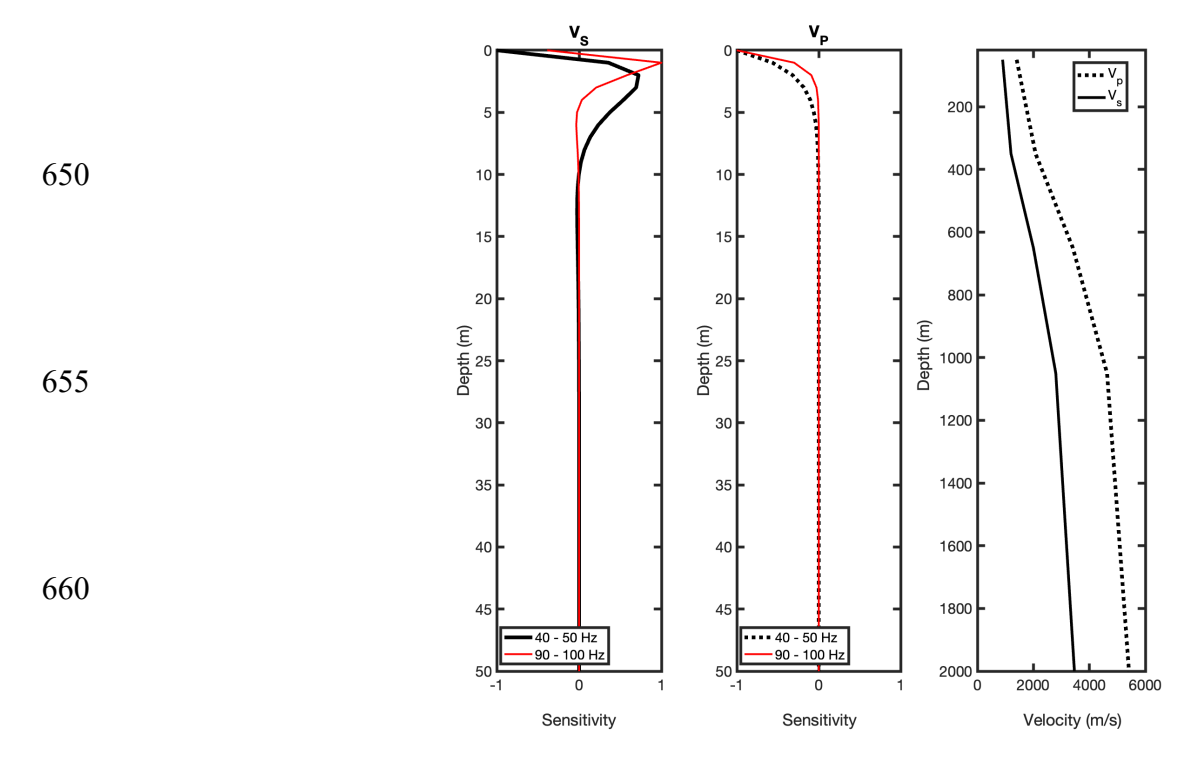


Figure A3. Normalized V_s and V_p depth sensitivity kernels for the fundamental mode of Rayleigh wave ellipticity at 40–50 Hz and 90-100 Hz frequency bands, computed using the Python package disba (Luu, 2021) and a reference velocity model constrained by tomographic studies of La Palma (e.g., Serrano et al., 2023; Cabrera-Pérez et al., 2023b).